JGR Solid Earth

RESEARCH ARTICLE
10.1029/2021JB022362

Stress Perturbations From Hydrological and Industrial Loads and Seismicity in the Salt Lake City Region

Xie Hu[1,2,3], Liang Xue[4], Roland Bürgmann[1], and Yuning Fu[4]

[1]College of Urban and Environmental Sciences, Peking University, Beijing, China, [2]Department of Earth and Planetary Science and Berkeley Seismological Laboratory, University of California Berkeley, Berkeley, CA, USA, [3]Department of Civil and Environmental Engineering, University of Houston, Houston, TX, USA, [4]School of Earth, Environment and Society, Bowling Green State University, Bowling Green, OH, USA

Key Points:

- The M5.7 Magna earthquake and its aftershocks, as well as persistent historical seismicity occurred in two clusters
- The elastic stresses near the hypocenter produced by nearby industrial loads exceed those from hydrological sources by two orders of magnitude
- The magnitude and sign of loading stresses resolved on receiver faults are sensitive to fault geometry, frictional coefficient, and location

Supporting Information:

Supporting Information may be found in the online version of this article.

Correspondence to:

X. Hu,
hu.xie@pku.edu.cn

Citation:

Hu, X., Xue, L., Bürgmann, R., & Fu, Y. (2021). Stress perturbations from hydrological and industrial loads and seismicity in the Salt Lake City region. *Journal of Geophysical Research: Solid Earth*, *126*, e2021JB022362. https://doi.org/10.1029/2021JB022362

Received 12 MAY 2021
Accepted 14 NOV 2021

Abstract The interconnection between anthropogenic and natural surface loads and seismicity continues to be poorly understood. The metropolitan Salt Lake City in Utah hosts various industrial, hydrological, and tectonic processes, including the Bingham Canyon mine and its associated tailings facility, precipitation and water storage at the surface and in aquifers, as well as the seismically active Wasatch Fault Zone. The March 18, 2020 M5.7 Magna earthquake occurred east of a mine tailings impoundment that receives ~60 million tons/yr of ore waste products since the early 1900s. Here we investigate the spatiotemporal elastic stress changes due to anthropogenic mass transfer and natural hydrological loading and unloading. Two local earthquake clusters host persistent microseismicity and the 2020 M5.7 Magna earthquake sequence. The amplitude and sign of the computed Coulomb stress changes at seismogenic depths strongly vary with the receiver fault geometry, the frictional coefficient, and the location, and can reach tens of kPa and ~1 kPa/yr due to the tailings loads, a substantial fraction of background tectonic loading. The long-term and seasonal stress changes from regional hydrological processes are only up to a few kPa. A lack of statistically significant seasonality in seismicity across Utah suggests a weak control by cyclic hydrological loads. Explicit knowledge of the fault architecture is essential to allow for seismic hazard assessment considering external stress loading.

Plain Language Summary The anthropogenic surface modifications in naturally hazardous environments have received relatively little attention due to their small dimensions and shallow locations. We note a compelling spatial correlation between a mine tailings impoundment and the March 18, 2020 M5.7 Magna earthquake, its aftershocks, and persistent earthquake clusters in the Salt Lake City region. This highly populated region hosts various industrial, hydrological, and tectonic processes. Here we characterize the spatiotemporal stress changes since the early 1900s due to the industrial and hydrological sources. The modeled elastic stress changes in the three dimensional subsurface vary in sign and magnitude, depending on the location, geometry, and frictional properties of active faults. Comprehensive characterization of fault architecture and seismic monitoring near sites of industrial production is warranted in critical geological and tectonic settings to ensure socioeconomic health and sustainable development.

1. Introduction

The complex nature of earthquakes and other geohazards has taught us that tectonic, hydroclimatic and anthropogenic factors can combine to cause fault failures in the crust. Changes in surface mass loads and subsurface pore pressure, such as from reservoir impoundment (e.g., Ge et al., 2009; Gupta, 2002; Talwani, 1997), open-pit and underground mining (e.g., Li et al., 2007; Pankow et al., 2014), extreme climate (e.g., Costain & Bollinger, 2010) and fluid injection and withdrawal (e.g., Ellsworth, 2013; González et al., 2012; Rubinstein & Mahani, 2015; Wetzler et al., 2019), may perturb the subsurface stress field especially if the transient loads can produce stressing rates comparable to the tectonic stresses. Regional hydrological loading has been recognized to modulate seismicity, often exhibited as an annual period in the number of earthquakes, such as in the Himalayas (Bettinelli et al., 2008), California (Amos et al., 2014; Johnson et al., 2017), the New Madrid Seismic Zone (Craig et al., 2017), southern Alaska (Johnson et al., 2020), and the East African Rift System (Xue et al., 2020). However, artificial surface load changes from landfills, construction, or quarrying may also affect the stress distribution (e.g., Ampuero et al., 2020; Qian et al., 2019), yet have been largely neglected due to their small dimensions.

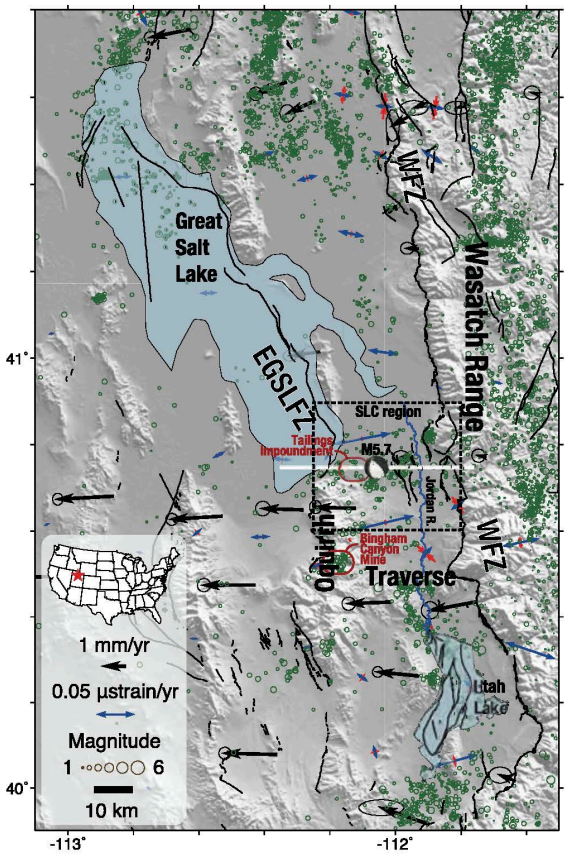

Figure 1. Map of north-central Utah along the eastern edge of the Basin and Range province. Black arrows, tipped with 95% confidence ellipses, show the GPS horizontal velocities in the stable North America reference frame (Herring et al., 2016). Blue and red arrow pairs show the extensional and contractional principal strain-rate axes, respectively, derived from GPS horizontal velocities. Green circles show the contemporary 1981–2018 earthquake catalog (>M0.8) archived at the University of Utah Seismograph Stations and their size represents the magnitude. Figure S1 in Supporting Information S1 shows event locations from historical earthquake catalogs. Black lines show Quaternary faults. The Wasatch Fault Zone extends along the frontal Wasatch Range. The East Great Salt Lake Fault Zone (EGSLFZ) underlies the Great Salt Lake. The March 18, 2020 M5.7 Magna earthquake occurred just to the east of the tailings impoundment near the southern shoreline of the Great Salt Lake. The source of the tailings, the Bingham Canyon mine, sits on the eastern flank of the Oquirrh Mountain. The Jordan River (blue line) connects the Great Salt Lake and Utah Lake. The EW trending white line shows the profile used in Figure 9. Dotted-line box denotes the Salt Lake City (SLC) region used in Figures 2, 7, and 8, and Figure S1 in Supporting Information S1 and referred to in the text. The extent of this figure is used to demonstrate the geographic locations of important features such as the epicenter, SLC region, tailings impoundment, Great Salt Lake, and Utah lake, and does not correspond to the bounds of the analyzed earthquake catalogs (see Sections 2.1 and 4.1 for details). The complete maps of earthquake catalogs in Utah are shown in Figure S1 in Supporting Information S1. Inset shows the location of the SLC study area in the contiguous U.S.

Salt Lake City (SLC) and the nearby Great Salt Lake are located in the hanging wall of the Wasatch Fault Zone (WFZ), forming the eastern margin of the Basin and Range province (Figure 1). The ~40-km SLC segment along the central WFZ has a vertical slip rate between 0.9 and 1.8 mm/yr, a recurrence interval of surface-breaking ruptures of 1,300–1,500 years, and the latest surface-rupturing event dates back to 1,300 ± 200 years B.P (DuRoss & Hylland, 2015; DuRoss et al., 2016). Most of the contemporary deformation across the eastern Basin and Range occurs in this Intermountain Seismic Belt (e.g., Chang et al., 2006). The Salt Lake basin also hosts the east-dipping West Valley Fault Zone (WVFZ) to the west of the Jordan River and subparallel to the WFZ, constituting a graben that hosts a dynamic confined aquifer (Hu & Bürgmann, 2020; Hu et al., 2018). To the south, the Traverse Mountains separate the Salt Lake basin from another remnant of prehistoric Lake Bonneville, the Utah Lake.

Of particular significance to the local economy and history, the Bingham mining district in the Oquirrh Mountains west of the Salt Lake basin has supported generations of SLC residents since its initial discovery around 1850 (Krahulec, 2018). It features the world's deepest (>970 m) man-made excavation and open-pit ore mine–the Kennecott's Bingham Canyon mine (e.g., Krahulec, 2018). Two massive rock avalanches, known as the Manefay landslides, occurred in the mine in April 2013, which dynamically triggered 16 small and shallow earthquakes within 10 days following the slope failure (Pankow et al., 2014). The open-pit mining operation officially started in 1906 and the tailings have been transported ~20 km north and deposited in an impoundment to the north of Magna, adjacent to the south shore of Great Salt Lake. The recent M5.7 Magna earthquake struck the metropolitan SLC region on 18 March 2020, when the residents sheltered in place at home during the COVID-19 pandemic. Intriguingly, the M5.7 event and its aftershocks occurred immediately east of the tailings dam, where historical microseismicity has also been clustered for many decades (Bowman & Arabasz, 2017; Hu & Bürgmann, 2020).

To address concerns about the potential impact of natural and anthropogenic load changes on seismic hazards, especially near dense population centers, we first collect the earthquake catalogs, quantify the anthropogenic mass transfer and the hydrological mass loading and unloading (Figure 2), and present a finite element model to compute elastic stress changes due to the different loading sources (Section 2). Then, we show the Coulomb stress changes at different timescales and the role of fault geometry and friction coefficient in the results (Section 3). Finally, we investigate the potential spatiotemporal correlations between the elastic stress changes induced by hydrological and industrial loads and the distribution of earthquakes in the SLC region since 1900 (Section 4). While seasonal and long-term stress changes from hydrological loads (lakes, aquifers, soil moisture, and snow) are small and do not appear to modulate seismicity in this area, more than one century of mining tailings accumulation from the Bingham Mine substantially modified the local stress in the hypocentral area of the 2020 Magna earthquake and nearby clusters of historic seismicity. However, the sign and magnitude of the stress changes are highly sensitive to the chosen receiver fault location, geometry, and frictional properties, and we emphasize the associated uncertainties in this study.

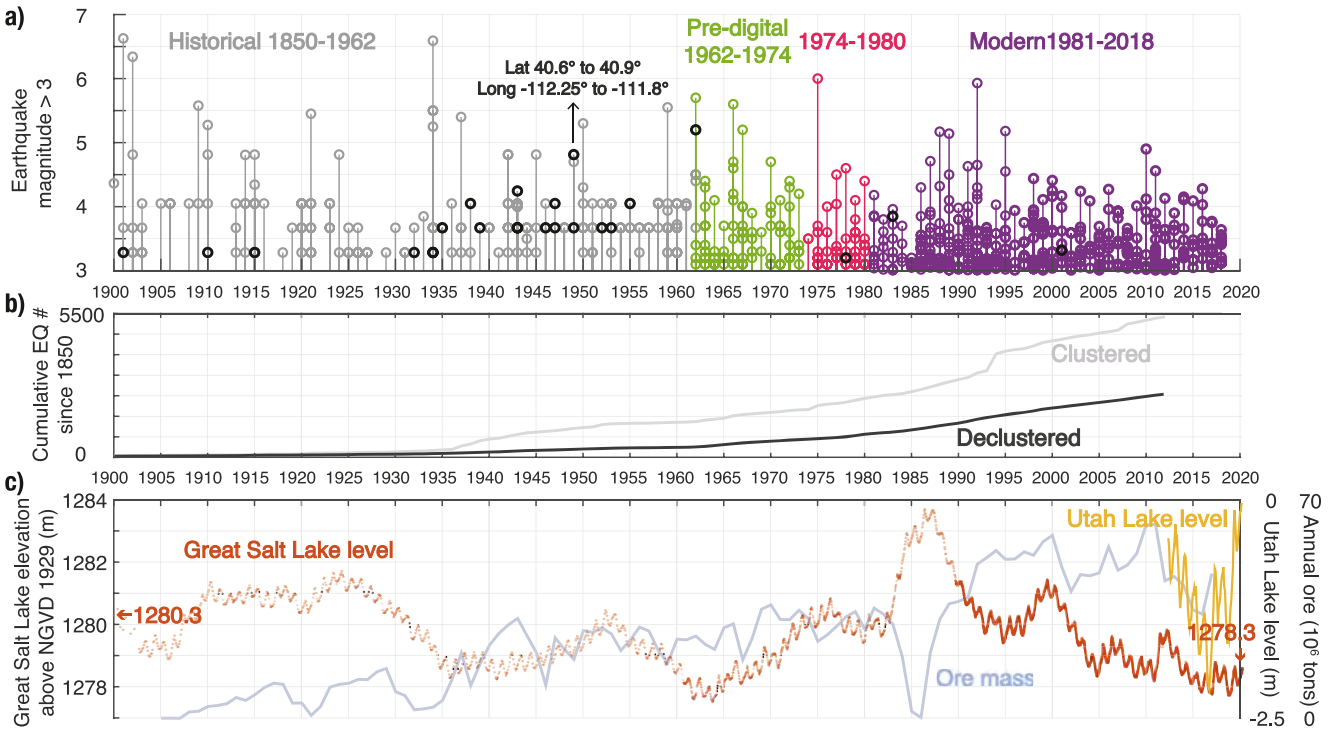

Figure 2. History of earthquakes and surface loads. (a) Historical, pre-digital, and modern earthquake catalogs of >M3 events (declustered) across Utah (36.75°–42.50° N, 108.75°–114.25° W) in colored circles, and in the Salt Lake City region (40.6°–40.9° N, 111.8°–112.25° W) in black circles. (b) The cumulative number of original (gray) and declustered (black) earthquakes from the 1850–2012 Uniform Moment Magnitude catalog from UUSS. (c) Time series of the Great Salt Lake level at Saltair Boat Harbor (orange), the Utah Lake level (yellow), the annual ore production (light blue). The Great Salt Lake level records are more frequent after the early 1990s and thus appear as a solid line.

2. Data and Methods

In this section, we describe the archived earthquake catalogs from the University of Utah Seismograph Stations (UUSS), the structure of the Bingham Mine tailings impoundment and the mass transfer from the mine site to the impoundment, the surface loading and unloading from the Great Salt Lake and Utah Lake levels, soil moisture, snow, and seasonal aquifer storage, as well as their coverage and spatio-temporal resolutions. We also document the finite element model used in the elastic stress computation.

2.1. Earthquake Catalogs

The UUSS archives one historical (1850–1962), two pre-digital (1962–1974 and 1974–1980), and one modern (1981–2018) earthquake catalogs for the Utah region (36.75°–42.50° N, 108.75°–114.25° W) (Figure S1 in Supporting Information S1). We consider both the large-scale, state-wide Utah region and the small-scale, basin-wide SLC region to investigate the temporal behaviors. Please refer to Section 4.1 for more information. The historical catalog includes 566 events from 1850 to June 1962, yet the information on event magnitudes and locations is insufficient to perform declustering (Figure S2 in Supporting Information S1). For the pre-digital and modern catalogs, we apply the Reasenberg declustering method (Lay & Wallace, 1995) implemented in the Zmap software (Wiemer, 2001). The pre-digital catalogs include 846 events from 1962 to 1974, of which 809 events were left after declustering (Figure S3 in Supporting Information S1). The modern UUSS seismographic network was installed in 1974 (Arabasz et al., 1992), resolving 4,765 events from 1974 to 1980, of which 3,669 were found to be independent (Figure S4 in Supporting Information S1). The modern catalog during 1980–2018 includes about 52.5k events with about 26k left after declustering (Figure S5 in Supporting Information S1). The magnitude of completeness and the associated coefficients are determined for consecutive 5-year windows and the entire period, and the results are similar (Table S1 in Supporting Information S1). Additionally, the Uniform Moment

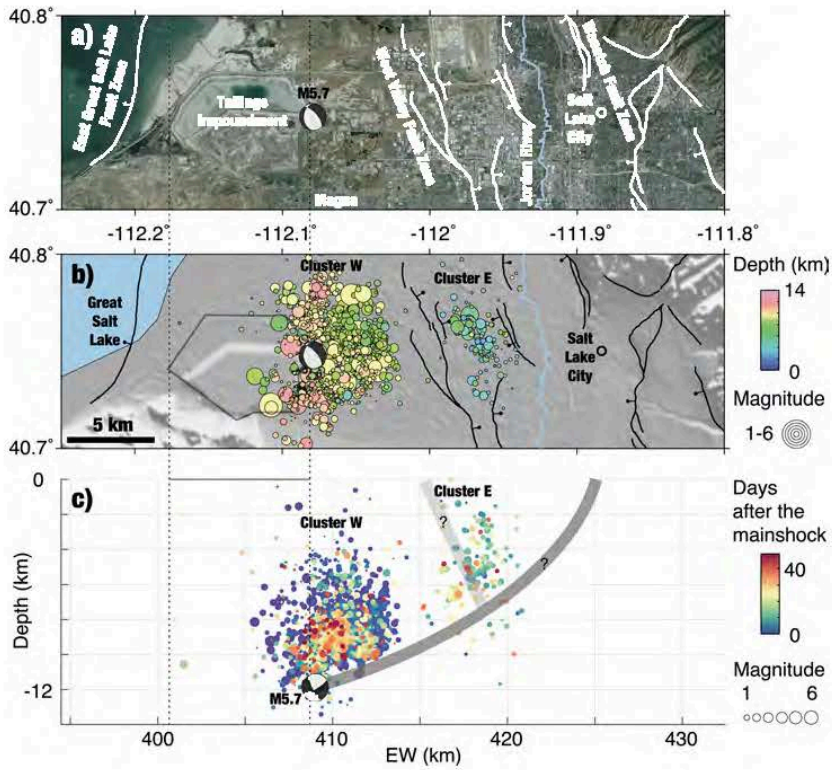

Figure 3. M5.7 Magna earthquake sequence in the central Salt Lake City region. (a) Aerial imagery of the study area. The mainshock occurred next to an 80-m-deep tailings impoundment. (b) The M5.7 Magna earthquake and its aftershocks. The white lines in (a) and black lines in (b) show the Quaternary faults including the west-dipping Wasatch Fault Zone (WFZ) and East Great Salt Lake Fault Zone, and the mostly east-dipping West Valley Fault Zone (WVFZ). The aftershocks are concentrated in cluster *W* and cluster *E* that are separated by the main strand of the WVFZ. (c) Side view of M5.7 event and its aftershocks. The size of the circles represents the magnitude, and the color denotes the number of days after the March 18, 2020 mainshock. The focal mechanism of the main shock that nucleated at a depth of 11.9 km comes from USGS; shown in side view in panel (c). The two vertical dashed lines indicate the bounds of the tailing impoundment. The thick gray lines give a schematic view of the inferred listric structure of the WFZ (Velasco et al., 2010) and the conjugate WVFZ, modified from Wong et al. (1995), DuRoss and Lund (2013), and Pang et al. (2020).

Magnitude Earthquake Catalog for 1850–2012 reports 5,388 clustered and 2,425 declustered events (Figure S6 in Supporting Information S1).

For the 2020 Magna earthquake sequence, a total of 2,017 events were detected after the mainshock from March 18 to May 6, 2020. The spatial distribution of the aftershock sequence shows two distinct clusters that we refer to as cluster *W* and cluster *E* based on their relative locations (Figures 3 and 4a). These two aftershock clusters appear co-located with event clusters in the pre-2020 catalogs (Figures 4b and Figure S1 in Supporting Information S1). By fitting a single plane to all relocated events in cluster *W*, Pang et al. (2020) inferred a strike of 159° and a dip of 21° with sub-clusters suggesting multiple west-dipping faults, and they reported no steeply east-dipping sub-clusters among these deeper aftershocks. Baker et al. (2021) used nodal arrays and machine learning techniques to produce a detailed aftershock focal mechanism catalog, dominated by variable normal-faulting mechanisms accompanied with some strike-slip events.

The earthquake catalogs compiled by UUSS recorded more than 20 earthquakes with $M > 3$ surrounding the tailings impoundment during 1900–2018 (black circles in Figure 2a). The largest pre-2020 earthquake in cluster *W* was a M5.2 event at a focal depth of ~10.7 km on September 5, 1962 (Figures 2a and Figure S1b in Supporting Information S1); no damage to the tailings impoundment was reported. Wong et al. (1995) proposed that

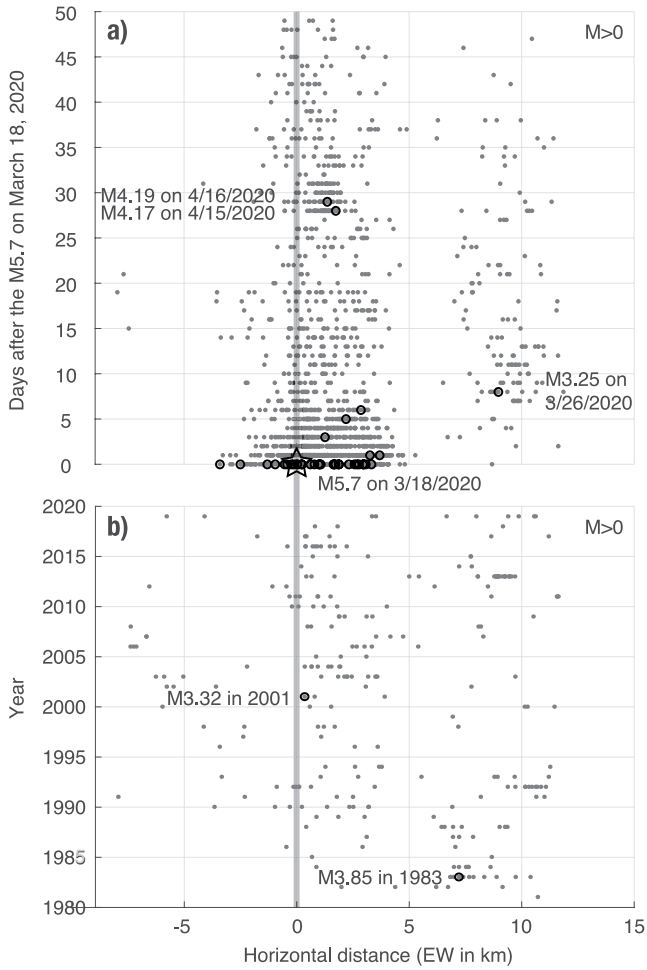

Figure 4. Earthquake occurrences in space and time within a ~10- by ~25-km rectangular area (shown in Figure 3) in central Salt Lake City region plotted with respect to EW horizontal distance from the mainshock epicenter. (a) Aftershocks of the M5.7 Magna earthquake between 3/18/2020 and 5/6/2020. (b) Background seismicity during 1981–2018.

a ~20-km-long, buried and east-dipping "Saltair structure" represents the source fault of the 1962 event, based on the distribution of a small number of aftershocks and a local gravity anomaly. Kleber et al. (2020) reprocessed the legacy gravity data and interpreted the "Saltair structure" to be a graben with its western bounding fault dipping to the east and its eastern bounding fault likely an extensional reactivation of the Ogden thrust fault. They found that the geometries and properties of the faults underneath the tailings impoundment are further complicated by the inferred Harkers fault and the Transverse fault zone.

Similar to the distribution of microseismicity since 1981 in the modern catalog (Figure S1d in Supporting Information S1) (UUSS; Figure 7 in Hu & Bürgmann, 2020), cluster *E* produced fewer aftershocks and lies at a shallower depth than cluster *W* (Figure 3). The WVFZ lies just west of cluster *E* where fault structures mainly dip steeply to the east (a strike of 346° and a dip of 63°; Pang et al., 2020; UUSS [@UUSSquake], 2020a), and may have jointly produced both long-term microseismicity and aftershocks. Pollitz et al. (2021) relied on the joint inversion of seismic waveform and geodetic observations to constrain the distributed coseismic slip on a west-dipping fault, followed by distributed afterslip on the up-dip extension of this fault and a conjugate, steeply northeast-dipping (319°/64°) fault.

Overall, previous studies (e.g., Baker et al., 2021; DuRoss & Hylland, 2015; Pang et al., 2020; Kleber et al., 2020; Pollitz et al., 2021; UUSS [@UUSSquake], 2020a; Wong et al., 1995) support a shallowly west-dipping listric WFZ at the bottom of cluster *W*, on which the M5.7 Magna Earthquake nucleated; however, the interpretations of structures in the hanging wall contained in the Saltair zone diverge and are often speculative. Given such complexity, we do not attempt to validate the exact geometric and kinematic characteristics of the fault system. Instead, to be inclusive, we consider two representative west- and east-dipping scenarios in two widely used Earth structures and broaden the uncertainty analysis to the complete range of permissible geometric and frictional parameters.

2.2. Mine Operations and Tailings Impoundment

The Oquirrh Mountains host the Bingham Canyon copper mine that started its production in the early 1900s (Hu et al., 2017, and references therein). A ~34-km^2 tailings impoundment was developed just south of the Great Salt Lake, consisting of a 20-km^2, now inactive south pond close to the residential area of Magna and a 14-km^2 north pond holding the tailings since ~2001 (Figure 3). The south pond has a 5-layer structure of spigotted tailings, soft tailings clay, deep whole tailings, Upper Bonneville clay, and interbedded sediments from the surface to a depth of 80 m (Hu et al., 2017 and references therein). The tailings embankment failed at least three times in 1941, 1964 and 1998 due to water intrusion and liquefaction. Continuous water pumping has been deployed to enhance the consolidation settlement and thus to stabilize the structures. In recent years, about 60 million tons of tailings have been deposited in the impoundment per annum (Tinto, 2019). Only a small fraction of the material is refined into copper and other precious metals (Krahulec, 2018). We consider the time series of annual production of raw ore until the latest reported records, from 1904-05 to 2017 (light blue line in Figure 2b) as the cumulative tailings load evenly distributed across the whole impoundment. An even larger volume of barren waste rock from the site has been deposited within a few km from the open-pit mine. After compiling all evidence, we assume that the mass reduction at the mine site equals the mass increase at the tailings pond.

2.3. Surface Loads From the Great Salt Lake and the Utah Lake

The prehistoric Lake Bonneville was the largest late Pleistocene pluvial lake in the region, reaching a maximum depth of 380 m and an area of ~52,000 km^2 (Gilbert, 1890). A catastrophic outburst flood about 14,500 years ago left three major remnants in the forms of the Great Salt Lake and the Utah Lake around Salt Lake Valley in northern Utah (Figure 1), and the almost dried-out Sevier Lake in western Utah (Gwynn, 1996). Lake Bonneville diminished dramatically after the last ice age. This abrupt postglacial unloading and associated viscoelastic rebound led to a faster slip rate and increased seismicity over the Wasatch region including the WFZ and WVFZ, as inferred from time-dependent stress modeling, Holocene to recent geologic, palaeoseismological, and geodetic data (Bills et al., 1994; Hetzel & Hampel, 2005).

We obtain the water level record of the Great Salt Lake at the Saltair Boat Harbor station (1847 to present; orange dots in Figure 2b) from USGS (https://waterdata.usgs.gov/nwis/inventory/?site_no=10010000), and that of the Utah Lake (2012 to present; yellow dots in Figure 2b) from the Bureau of Reclamation database (https://www.usbr.gov/rsvrWater/HistoricalApp.html). The lake levels vary seasonally, reaching their maxima around May due to abundant recharge from mountain snowmelt. The lake levels also vary over multi-year time scales due to climate variabilities, including drought and substantial lake drawdowns from the late 1980s to early 1990s, from the late 1990s to early 2000s, and most recently from 2012 to 2016.

2.4. Loads From Soil Moisture, Snow and Aquifer Water

We obtain the monthly soil moisture estimates from the Noah North American Land Data Assimilation System (NLDAS) land surface model at a coarse resolution of 0.125° (Mitchell et al., 2004). We also collect snow water equivalent thickness estimates from NLDAS and the SNOw Data Assimilation System (SNODAS) with a spatial resolution of ~11 km (Figure 5). We calculate the monthly averaged SNODAS data to keep consistency with the temporal resolution of NLDAS data. The snow estimates from the two models show some disparities in magnitude, but the distribution is generally consistent. The stresses generated by the two snow-load models are similar due to the long-wavelength nature of the stress field. We use the results from SNODAS for our analysis because NLDAS has been shown to underestimate the snow-load component (e.g., Argus et al., 2014). We consider the soil moisture and snow loads covering a wide region spanning Long. 107° to 117°W and Lat. 38° to 45°N to capture the full long-wavelength load contributions. Each summer, snow almost vanishes everywhere except for a few small high-altitude areas. The seasonal changes in water equivalent thickness from the soil moisture and snowfall are each up to ~0.5 m (Figure 5) (Argus et al., 2014; Mitchell et al., 2004).

A dynamic aquifer in the graben between the WVFZ and WFZ is characterized by cyclic seasonal discharge/recharge processes (Hu et al., 2018). From the first-order correlation between the seasonal groundwater level changes and the poroelastic displacements of the aquifer skeleton, Hu and Bürgmann (2020) estimated a water equivalent thickness change of less than one meter and a corresponding seasonal volume change of 0.03–0.06 km^3, which allows us to further explore the seasonal loading effect from this local hydrological unit embedded in the graben.

2.5. Finite Element Loading Model and Stress Computation

To characterize both the natural and anthropogenic loading effects on the SLC region, we consider hydrological loads from the Great Salt Lake, Utah Lake, snow, soil moisture, and the local aquifer, as well as the artificial loads from the tailings. We obtain the annual mass loading at the tailings impoundment and the corresponding mass unloading at the mine site from available records (Krahulec, 2018), and then we compute the associated spatio-temporal stress variations on a multi-annual scale. Daily to monthly estimates of the hydrological loads are available, which allows us to explore the associated spatio-temporal stress variations also on the seasonal scale. The stress distributions from snow and soil moisture represent regional effects dominated by seasonal variations, and the aquifer load also does not exhibit appreciable multi-annual changes (Hu & Bürgmann, 2020). Therefore, we only focus on their seasonal variations.

We apply a finite-element model to compute the stress field changes using the quasi-static code PyLith (Aagaard et al., 2013). We construct a fine mesh (2-km cells for 80 × 80 × 60 km) for modeling the tailings impoundment and copper mine load changes, a moderate mesh (5-km cells for 200 × 250 × 60 km) for modeling the

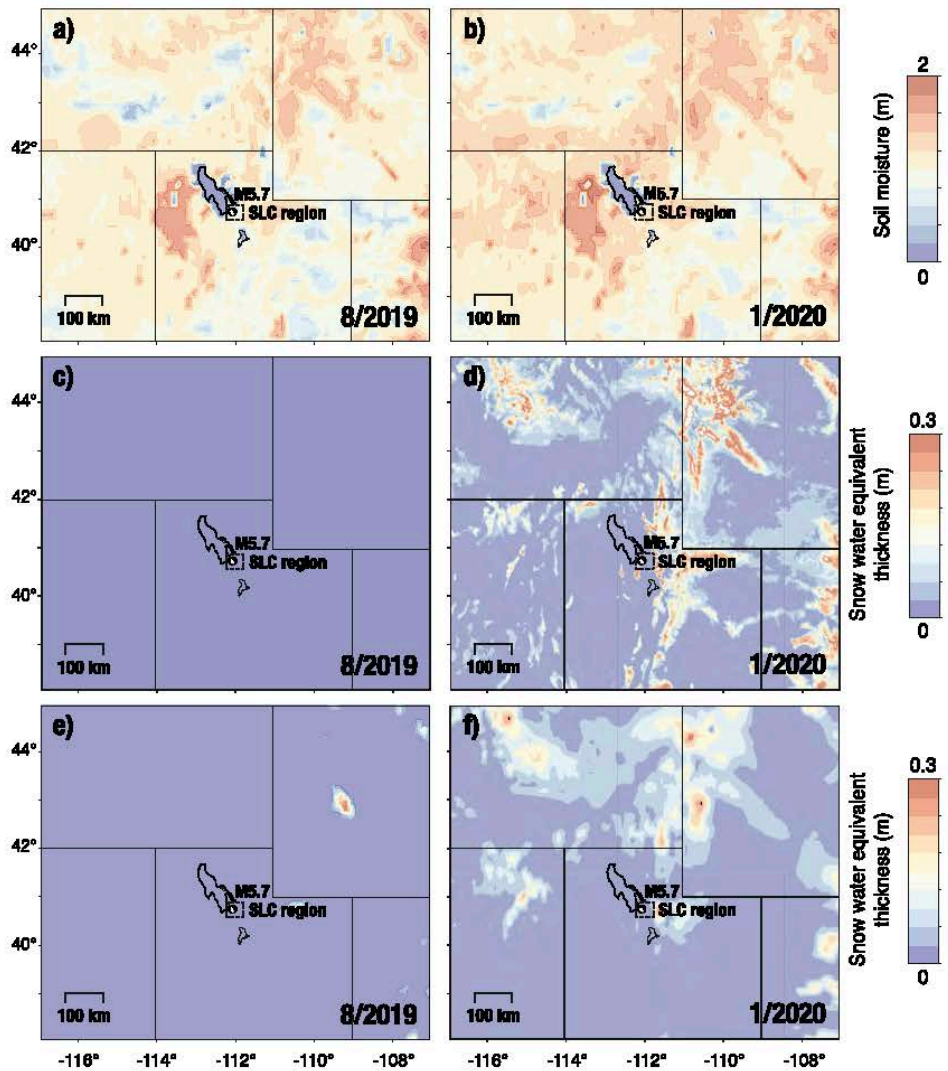

Figure 5. Regional hydroclimatic data (Long. 107° to 117°W and Lat. 38° to 45°N). (a–b) Equivalent water thickness of soil moisture from the North American Land Data Assimilation System (NLDAS) model. (c–d) Snow water equivalent thickness from the SNODAS model. (e–f) Snow water equivalent thickness from the NLDAS model in representative summer (8/2019) and winter (1/2020) months. The focal mechanism and the dotted-line box show the locations of the epicenter of M5.7 Magna earthquake and the SLC region.

Great Salt Lake and the aquifer, and a comparatively coarse mesh (20-km cells for $850 \times 800 \times 600$ km) for the contributions by Utah Lake and the long-wavelength soil moisture and snow loads (Figure 6). We enforce the corresponding normal traction within the boundaries of the target sources. We apply the elastic structure derived from seismic velocity models to the mesh. The seismic Vs. and Vp velocities in the Western U.S. (WUS) model (Herrmann et al., 2011) differ slightly from the global Preliminary Reference Earth Model (PREM; Dziewonski & Anderson, 1981; Figure S7 in Supporting Information S1). Since WUS is specifically designed for the western United States including Utah and has been adjusted to fit surface-wave dispersion curves (Herrmann et al., 2011; Whidden & Pankow, 2012) and also chosen in the recent seismic relocation by UUSS (Pang et al., 2020), we focus on using an elastic Earth structure constrained by the seismic velocities defined in the WUS model and the densities from the global PREM. Results using seismic velocities defined in the PREM model are available in the

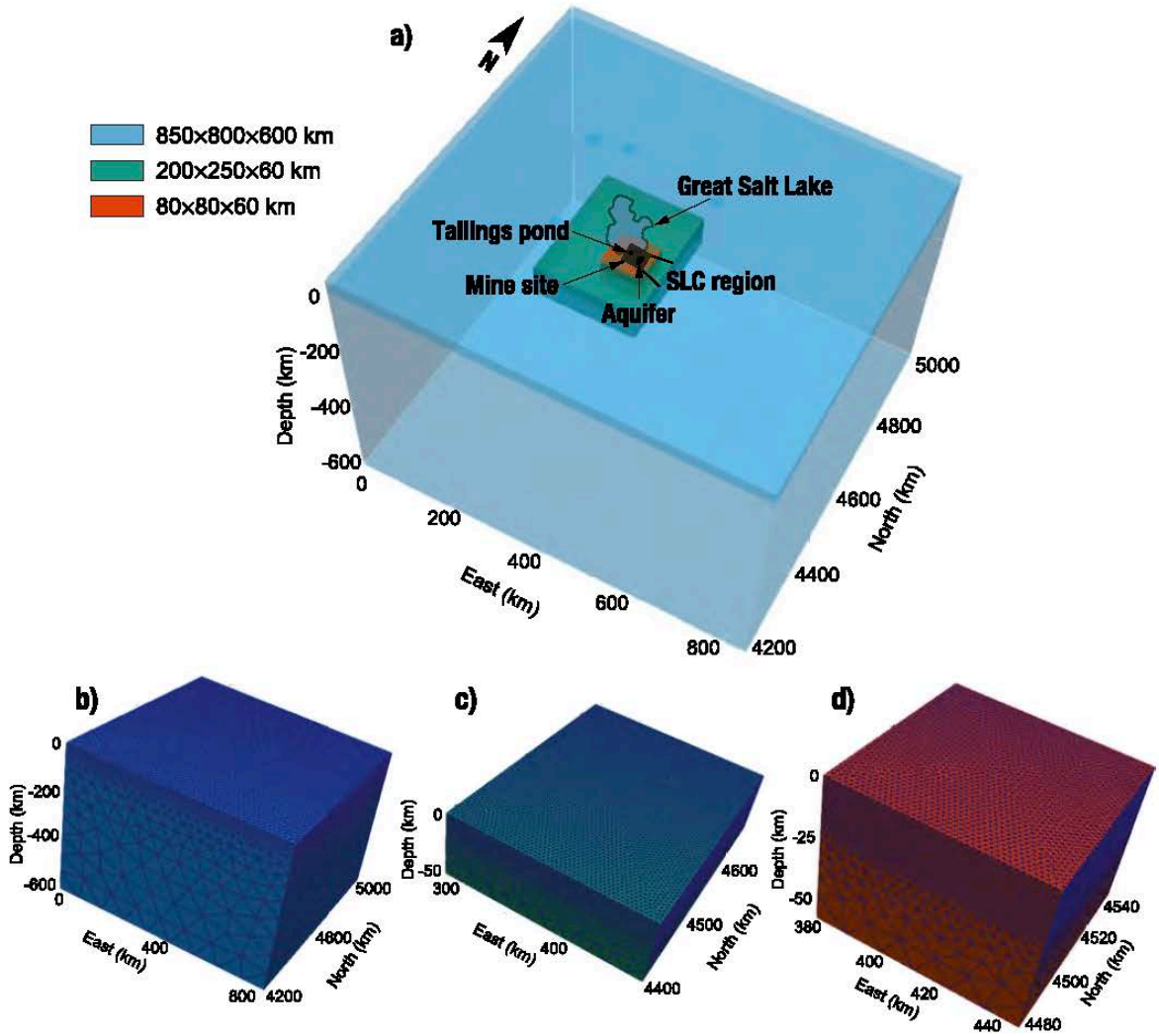

Figure 6. Regional finite element model (Long. 107° to 117°W and Lat. 38° to 45°N). (a) Three meshes and the geographic locations of the Great Salt Lake, aquifer, tailings pond, and the Bingham Canyon mine. (b) to (d) The dimensions of the tetrahedral meshes. Cell sizes are 20, 5, and 2 km for the coarse, moderate, and fine meshes, respectively.

supplementary information (Figures S9–S11 in Supporting Information S1). We consider the surface mass normal load as a Neumann boundary condition on the mesh top surface. The model domain extends between Long. 107° to 117°W and Lat. 38° to 45°N, and down to 600 km depth, and we fix these lateral and bottom boundaries to zero displacement. Our area of interest is far from the boundaries so that the edge effects in our target area are minimal.

Since the M5.7 event and its aftershocks occurred in a complicated seismogenic regime associated with listric, synthetic, antithetic, and other conjugate faults, we consider a west-dipping WFZ receiver-fault geometry striking 182° and dipping 29° (from linear fit through the relocated aftershocks from March 18 through March 24 in cluster *W*; UUSS [@UUSSquake], 2020b), and an east-dipping WVFZ scenario striking 320° and dipping 65° (based on the east-dipping nodal planes of the M5.7 and large aftershocks reported by USGS, almost subparallel to the principal faults of the WVFZ) for the 3D numerical stress computations. We resolve the stress tensors derived from surface loading, and project the tensors to the respective receiver fault planes. Then we solve for the

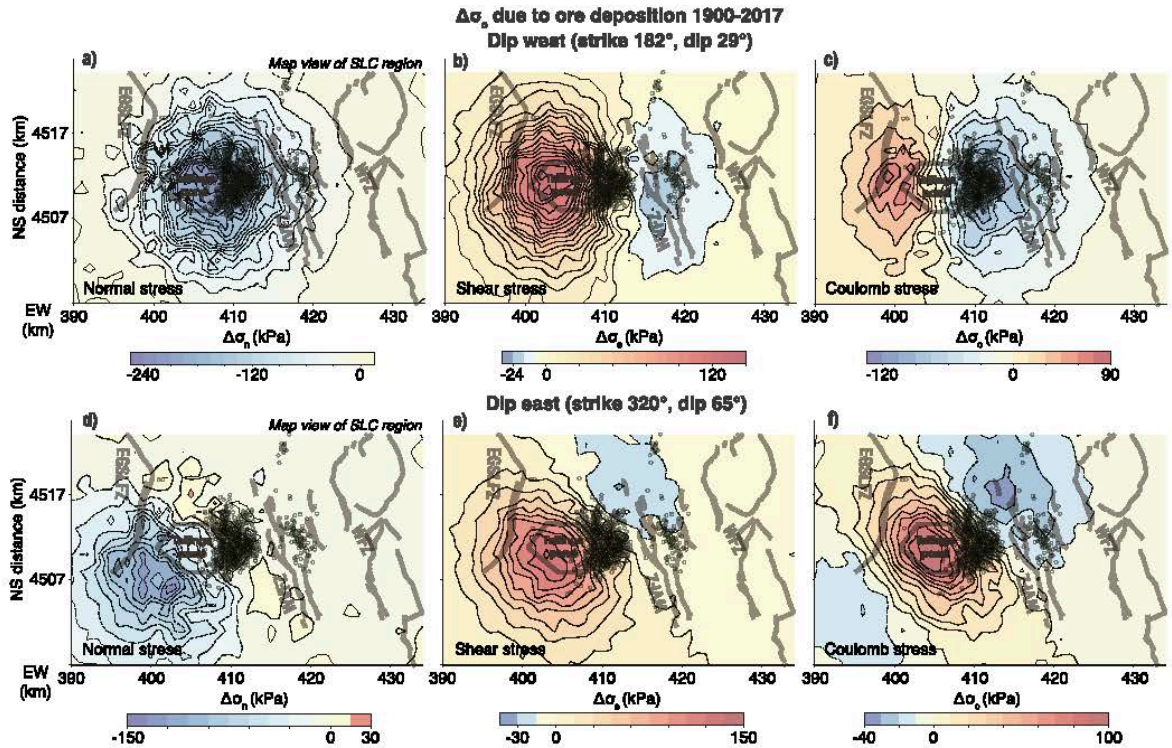

Figure 7. Salt Lake City (SLC) region map views of the normal, shear and Coulomb stress changes $\Delta\sigma_c$ due to ore transport from the mine to the tailings impoundment considering a strike of 182° and dip of 29° (to west) and a strike of 320° and dip of 65° (to east) in a pure normal faulting regime. Here we apply the seismic velocity profile defined in the WUS model as the Earth structure. Bold gray lines show the faults (Figure 1). Polygons outline the tailings impoundment. Circles show the Magna earthquake aftershocks. The change in normal stress is positive when the receiver fault is unclamped. Positive shear stress changes encourage normal-faulting. The map extent corresponds to the SLC region marked by the dotted-line box in Figure 1.

normal and shear-stress components and use an effective friction coefficient of 0.4 to compute the Coulomb stress changes assuming pure normal faulting (Figure 7). It is believed that positive Coulomb stress changes advance the occurrence of future earthquakes, and negative ones delay them (e.g., Freed, 2005). The stress interactions can also influence the distribution of slip when an event occurs (e.g., Johanson & Bürgmann, 2010). Figure 7 and Figure S8 in Supporting Information S1 show the cumulative normal, shear and Coulomb stress changes due to ore transport from the mine to the tailings impoundment for two representative fault geometries in map and cross-section views, respectively. We note that, besides the fault configuration and the elastic Earth structure, the fault-frictional properties, hydromechanical coupling, and the possible uncertainties in the mass load can also influence the stress estimation (e.g., Freed, 2005). We consider two Earth structures and depict the uncertainties statistically due to fault geometries and friction coefficient in Section 3.2.

3. Results

We use the finite element model to compute the elastic stress changes due to the different sources of loading and unloading documented in Section 2. To compare the Coulomb stress changes $\Delta\sigma_c$ due to different loading sources, we extract 2D horizontal maps of stress changes at a depth of 9 km (e.g., Figure 8), and we also focus on a ~45-km-long EW cross section (e.g., Figure 9) overlapping with the southernmost part of the Great Salt Lake, the tailings pond, the hypocenter of the mainshock, alluvial basin, and WVFZ and WFZ from west to east (white line in Figure 1).

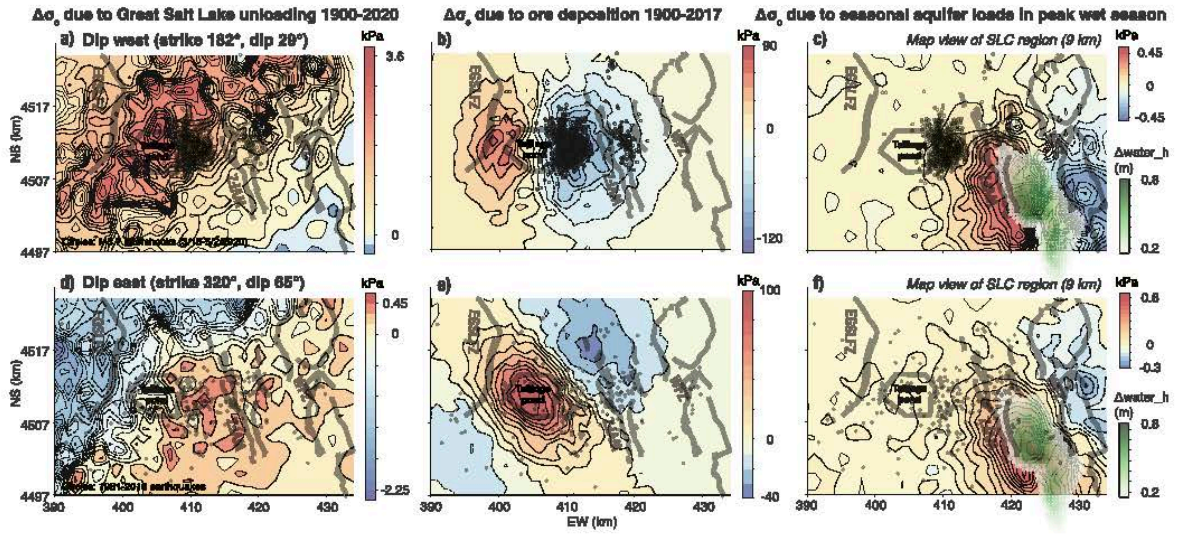

Figure 8. Salt Lake City (SLC) region map views of the Coulomb stress changes $\Delta\sigma_c$ associated with long-term Great Salt Lake and tailings loads, as well as seasonal aquifer load changes. Here we apply the seismic velocity profile defined in the WUS model as the Earth structure. Bold gray lines show the faults (Figure 1). Polygons outline the tailings impoundment. First column (a), (d) shows $\Delta\sigma_c$ due to the Great Salt Lake level decrease since 1900 (USGS). Second column (b), (e) shows $\Delta\sigma_c$ due to the ore deposition at the tailings impoundment from 1905 to 2017 (Krahulec, 2018). Third column (c), (f) shows $\Delta\sigma_c$ due to the seasonal aquifer water change in the peak wet season (greenish dots) (Hu & Bürgmann, 2020). The first row considers a receiver fault with strike of 182° and dip of 29° (to the west) in a pure normal faulting regime; circles show the M5.7 Magna earthquake aftershock locations. The second row considers a receiver fault with a strike of 320° and dip of 65° (to the east) in a pure normal faulting regime; circles show the 1981–2018 earthquake locations. The computed Coulomb stress at a specific location depends on the assumed geometry of the receiver fault and the frictional coefficient at that location. Figure 9 applies the same panel sequence. Figure S9 in Supporting Information S1 shows the equivalent plots using the 1D elastic earth structure based on the PREM model. The map extent corresponds to the SLC region marked by the dotted-line box in Figure 1.

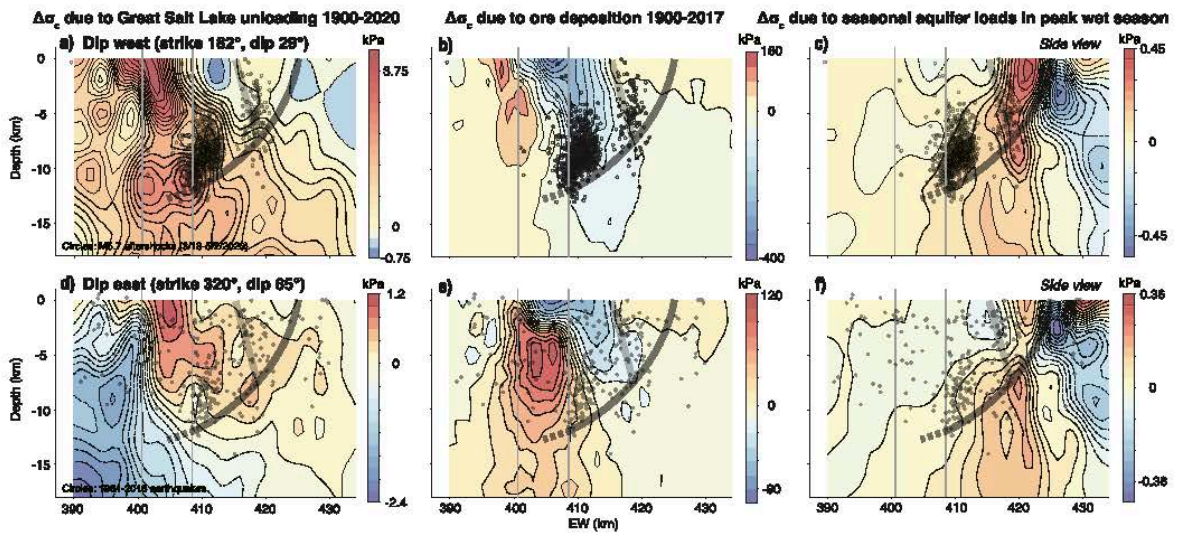

Figure 9. Salt Lake City region EW cross sections of the Coulomb stress changes $\Delta\sigma_c$ along the white line in Figure 1 associated with long-term Great Salt Lake and tailings loads, as well as seasonal aquifer load changes. Bold gray lines show a schematic view of the inferred faults (Figure 3c). Vertical gray lines at the top show the edges of the tailings pond. The hypocenter is in the deep part of the W-dipping fault. Please refer to Figure 8 for the panel sequence. The layered elastic Earth structure is from the Western U.S. seismic velocity model. Figure S10 in Supporting Information S1 shows the equivalent plots using the 1D elastic earth structure based on the PREM model.

3.1. Long-Term Coulomb Stress Changes

Though small in dimensions, the ore transport from the mine 20-km north to the tailings pond from 1905 to 2017 generated more than 100 kPa of Coulomb stress change on both the west- and east-dipping receiver faults in the upper few km of the crust and tens of kPa at 9 km depth (Figures 8b, 8e, 9b, and 9e), two orders of magnitude larger than the hydrological sources. The changes in Coulomb stress are opposite in sign in the seismogenic zone for the west and east dipping scenarios, as a result of the competing effects of normal and shear stresses (Figure 7 and Figure S8 in Supporting Information S1). Specifically, the ore deposition results in a $\Delta\sigma_c$ decrease by -52 ± 7 kPa in cluster *W* for the west-dipping geometry, whereas there is a $\Delta\sigma_c$ increase by 40 ± 12 kPa for the east-dipping geometry, calculated as the average and one standard deviation of stress change values within 2 km of the hypocenter at 9 km depth (Figures 8b, 8e, 9b, and 9e). In the case of the low-angle west-dipping geometry of the WFZ in the lower cluster *W* (e.g., Pang et al., 2020), the decreasing $\Delta\sigma_c$ suggests the tailings loads discourage the failure due to the increased normal stress (Figure 7). Beyond that, the area with a positive $\Delta\sigma_c$, just to the west of the impoundment and clusters is near the edge of the Oquirrh Mountain. We believe that there is no evident fault activity in this zone and thus there is a lack of seismicity through the earthquake cycle including during the Magna sequence.

The Great Salt Lake level was ∼1280.3 m (above NGVD 1929) on 1/17/1900 and ∼1278.3 m on 1/16/2020 (arrows in Figure 2b). We compute the long-term net decrease of the lake load by 2 m from 1900 to 2020 based on the product of the Great Salt Lake area, the lake level decrease in height, and the water density. The finest resolution of our finite model mesh is 2 km. We do not consider the shoreline migration with time considering the change in area is a small fraction compared to the large lake area. The lake unloading unclamps the fault and results in a net increase of $\Delta\sigma_c$ by ∼3 kPa in cluster *W* and ∼0.25 kPa in cluster *E* for the 29° west-dipping geometry, and by ∼0.4 kPa in both clusters for the 65° east-dipping geometry (Figures 8a, 8d, 9a, and 9d). During the historical high stand of Great Salt Lake in 1986 (1283.7 m, Figure 2), slip-discouraging stress levels in clusters *E* & *W* reached as high as −4.2 kPa.

3.2. Sensitivity Analysis on Fault Geometry and Friction Coefficient

We investigate the sensitivity of the modeled normal, shear and Coulomb stresses $\Delta\sigma_c$ at 9 km depth of the M5.7 event from the tailings load to the strike (0°–360°), dip (0°–90°), and the friction coefficient μ (0.1–0.8) in a pure normal-faulting regime, with one variable changing and the other two fixed, respectively (Figure 10). Results show that these parameters jointly affect the sign and magnitude of the consequent $\Delta\sigma_c$. Various combinations of strike and dip can yield positive $\Delta\sigma_c$ near the M5.7 hypocenter, such as (i) when the westward dipping angle is greater than 38° at a strike of 182°, and when the eastward dip is between 6° and 75° at a strike of 320°, considering $\mu = 0.4$ (Figures 10a and 10d); (ii) when strike <110° or >230° at a shallow dip of 29°, and any strike angles at a steep dip of 65°, considering $\mu = 0.4$ (Figures 10b and 10e); (iii) when $\mu < 0.2$ for a strike of 182° and a dip of 29° and any μ for a strike of 320° and a dip of 65° (Figures 10c and 10f). The stress changes at the hypocenter of the M5.7 event from the anthropogenic load redistribution can reach 100 kPa. However, the sign and amplitude strongly depend on the location, geometries, and friction coefficient of the receiver fault (e.g., Hardebeck et al., 1998; Harris & Simpson, 1992).

We also compare the stress fields for the layered elastic Earth structures defined in the WUS and PREM models. The consequent spatial patterns of the loading stresses are nearly identical, and the magnitudes are in the same order of magnitude (Figures 8 and Figure S9, S10 in Supporting Information S1).

3.3. Seasonal Coulomb Stress Changes

Hydrological loading has been well documented in modulating the stress field and seismicity in tectonically active regions, often following annual cycles with distinct seasons. We evaluate the amplitude of annual stress changes near the Magna earthquake, so we can examine if the periodic stress changes produce a resolvable seasonality in seismicity. During the wet season, the shallow aquifer (160 km^2 in area and 600 m in depth) contributes a decrease in $\Delta\sigma_c$ to its east and an increase in $\Delta\sigma_c$ to its west with a peak amplitude of ∼0.5 kPa at seismogenic depths for both considered fault geometries (Figures 8c, 8f, 9c, and 9f), and an opposite $\Delta\sigma_c$ occurs during the dry summer and fall. Cluster *W*, which is ∼10 km northwest of and ∼10 km below the shallow aquifer, encounters a negligible $\Delta\sigma_c$. Cluster *E* is closer to the aquifer and experiences ∼0.3 kPa changes in $\Delta\sigma_c$ for the

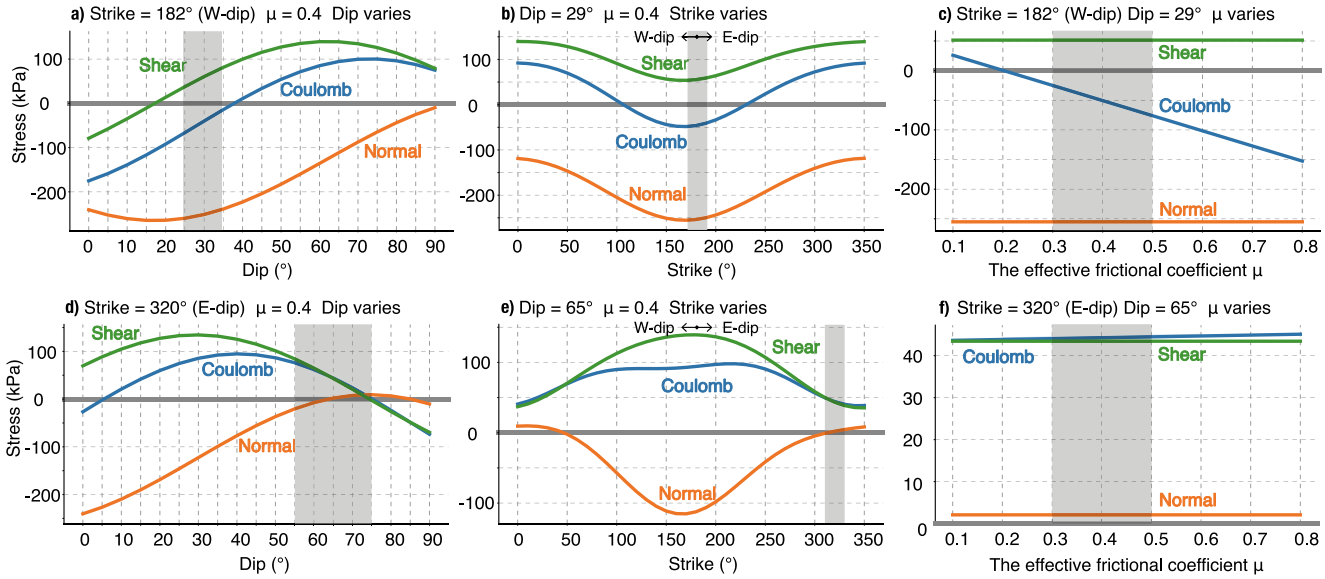

Figure 10. Stress changes at the M5.7 hypocenter due to tailings pond loading and mine unloading considering varying strikes, dips, and the effective coefficient of friction μ in context of pure normal faulting (rake = −90°). (a) Strike at 182°, μ equals 0.4, and variable dip to the west. The shaded area shows the dips within 29° ± 10°, which we consider to be a realistic range for the Magna earthquake sequence based on published studies discussed in the text. (b) Dip at 29°, μ equals 0.4, and variable strike. The shade area shows the strike within 182° ± 10° as more realistic for the Magna earthquake sequence. (c) Strike at 182°, dip at 29° (to the west), and variable μ. Shade shows μ within 0.4 ± 0.1 as more realistic for the Magna earthquake sequence. (d) Strike at 320°, μ equals 0.4, and variable dip to the east. Shade shows the dip within 65° ± 10° as more realistic for the Magna earthquake sequence. (e) Dip at 65°, μ equals 0.4, and variable strike. Shade shows the strike within 320° ± 10° as more realistic for the Magna earthquake sequence. (f) Strike at 320°, dip at 65°, and variable μ. Thick gray horizontal lines denote zero stress change. Shade shows μ within 0.4 ± 0.1 as more realistic for the Magna earthquake sequence.

east-dipping scenarios. We also consider the elastic loading sources from the Great Salt Lake, Utah Lake, soil moisture, and snow water for a one-year period (i.e., 3/2019-2/2020), and compute $\Delta\sigma_c$ at the M5.7 hypocenter for the west- (Figures 11a) and east-dipping geometry (Figures 11b). The elastic loads from the Great Salt Lake and Utah Lake present similar phases in Coulomb stress with a peak in September. Decrease in soil moisture and near absence of snow cover during July to October introduces months of low Coulomb stress in the hypocentral zone in cluster *W*.

4. Discussion

Here we investigate the degree of correlation between seismicity and loading-induced Coulomb stress changes at seasonal and multiannual timescales and spatial domain. We also demonstrate the limitations and challenges of this study.

4.1. Insignificant Seasonal Modulation of Seismicity

The seasonal peak-to-peak amplitudes of the elastic stress at the M5.7 hypocenter from the hydrological sources are small. The stress peaks in the fall at 1.08 kPa from the Great Salt Lake and 0.02 kPa from Utah Lake, partially canceled by the contemporary lows from the sources of soil moisture, snow, and the aquifer, resulting in a net amplitude of 0.44 kPa with more than one peak per annum for the shallow west-dipping fault at the M5.7 hypocenter (Figure 11a). Alternatively, the east-dipping fault scenario results in a net peak-to-peak amplitude of 0.24 kPa from different temporal phases (Figure 11b). For comparison, in California the periodic non-tectonic hydroclimatic sources contribute to a seasonal $\Delta\sigma_c$ in the range of 0.5–2 kPa on the fault systems adjacent to the Sierra Nevada, which may increase the seismicity by ∼10% when aligned with the background stress (Johnson et al., 2017).

We have considered both the large-scale, state-wide Utah region and the small-scale, basin-wide SLC region and all available catalogs (one historical 1850–1962, two pre-digital 1962–1974 and 1974–1980, and one modern 1981–2018 earthquake catalogs) to investigate the temporal behaviors. The reason for considering the larger

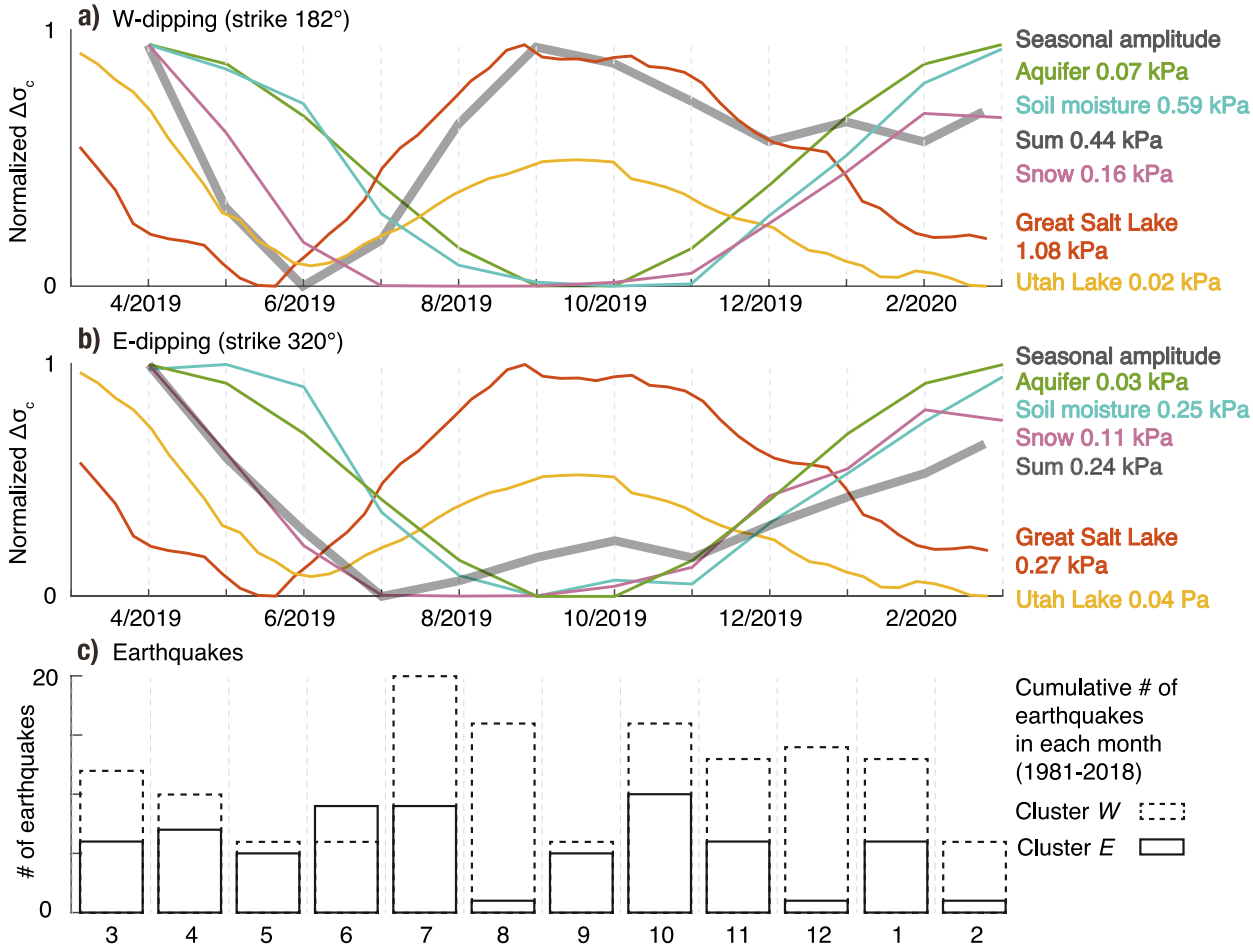

Figure 11. Annual variations in stress and the number of earthquakes in two clusters. Normalized seasonal Coulomb stress changes $\Delta\sigma_c$ at the hypocenter of the 2020 M5.7 Magna earthquake due to different hydrological loading sources during a one-year period (3/2019 to 2/2020) preceding the Magna earthquake. (a) For a strike of 182° and west-dipping of 29° fault geometry. (b) For a strike of 320° and east-dipping of 65° fault geometry. Here we apply the seismic velocity defined in the WUS model to describe the Earth structure. The seasonal amplitudes of stress changes from each loading source are labeled on the right. (c) Cumulative number of earthquakes in each month of the year (1981–2018) for clusters *E* & *W* shown in Figure 2b, modified from Hu and Bürgmann, 2020.

scale (data used in this study: Long. 107° to 117°W and Lat. 38° to 45°N; see Section 2.4) is because we would like to document any regional variations in seismicity that may be associated with the annual water loading (e.g., Johnson et al., 2017). The reason for focusing on the local small-scale loads is because the tailings pond and aquifer are localized in the basin very close to the epicentral area of the Magna earthquake. However, we conclude that there is no evidence of seasonal variation in seismicity in the UUSS catalog data spanning Utah (Figures S2–S5 in Supporting Information S1) or in the SLC region including clusters *E* & *W* (Figures 11c; Hu & Bürgmann, 2020). We believe that different choices of the spatial extent would not alter the finding that there is no demonstrable seasonality in seismicity using the existing catalogs. The use of modern detection methods, such as template matching and machine learning, may help further explore hydrological modulation of seismicity. More detailed spatio-temporal evaluation of the regional seasonal stress field and seismicity data would be needed (e.g., Johnson et al., 2017) to further explore evidence of hydrological modulation of seismicity across the state.

4.2. Importance of Long-Term Stress Perturbations

For a more quantitative comparison of the external stress perturbations and background tectonic loading, we focus on the long-term time frame from 1900 when the data of both the ore tailings mass and the Great Salt Lake level changes are available. The Great Salt Lake levels have fluctuated on a multi-annual timescale in response to prolonged climate variations, yet the consequent $\Delta\sigma_c$ near the Magna earthquake hypocenter have been modest

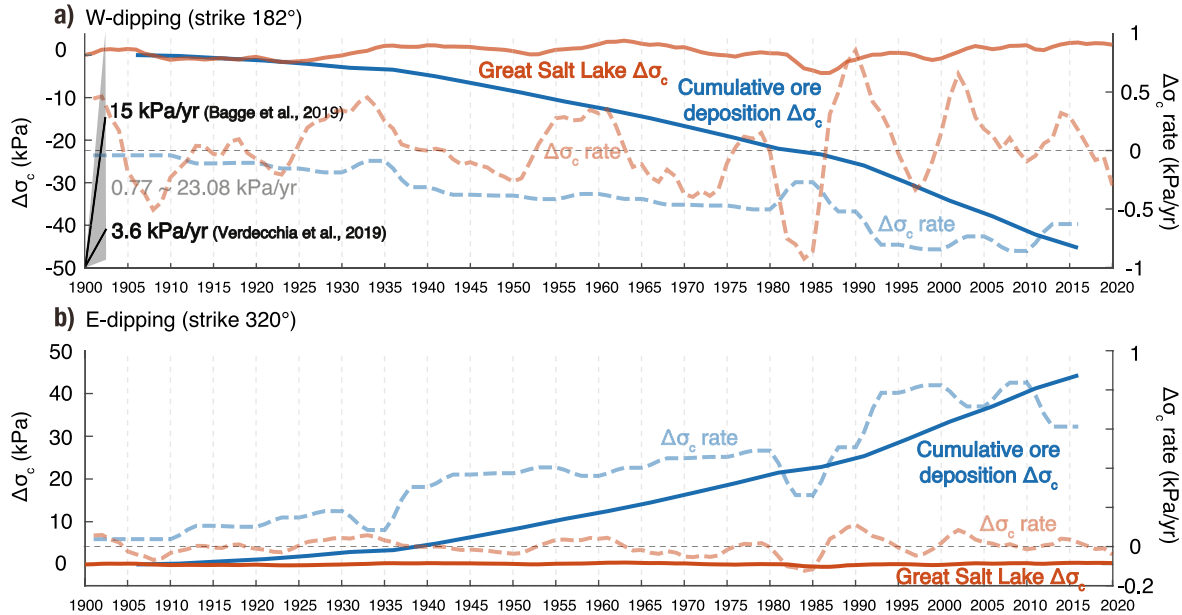

Figure 12. Multi-year evolution of Coulomb stress changes $\Delta\sigma_c$ and annual rates of $\Delta\sigma_c$ at the hypocenter of the 2020 M5.7 Magna earthquake due to ore deposition (blue solid and dashed lines) and Great Salt Lake load (orange solid and dashed lines), from 1900 to 2020. (a) For a strike of 182° and west-dipping of 29° fault geometry. (b) For a strike of 320° and east-dipping of 65° fault geometry. Black lines in (a) represent the reported tectonic loading rates (Bagge et al., 2019; Verdecchia et al., 2019) and gray-shaded area indicates the range of loading rates based on our back-of-the-envelope estimate, assuming a recurrence interval of 1,300 years (DuRoss & Hylland, 2015) and earthquake stress drops from 1 to 30 MPa.

($\pm$4 kPa). The $\Delta\sigma_c$ rate can occasionally reach $\pm$0.9 kPa/yr for the west-dipping scenario (orange lines in Figure 12a), while the $\Delta\sigma_c$ and its rate are only $\pm$0.5 kPa and $\pm$0.1 kPa/yr for the east-dipping scenario (orange lines in Figure 12b).

Unlike the cyclic loading and unloading from the hydrosphere, the tailings ponds represent a cumulative increase in load since 1900 (Krahulec, 2018). By the latest reported record in 2017, $\Delta\sigma_c$ from the tailings near the Magna hypocenter decreased by 52 $\pm$ 7 kPa assuming the west-dipping geometry, and the negative stressing rate increased to $-$0.8 kPa/yr for most years after 1990 (blue solid and dashed lines in Figure 12a). In contrast, for the east-dipping geometry, the increase of $\Delta\sigma_c$ and its rate amount to 40 $\pm$ 12 and 0.8 kPa/yr at 9 km depth (blue solid and dashed lines in Figure 12b). Note that the high cumulative stress occurs at shallower depths and just below the tailings impoundment. When applying the seismic velocity defined in the PREM as the Earth structure, the time-series of stress variations are similar (Figure S11 in Supporting Information S1).

The external stress and stressing rate changes from anthropogenic and hydrological loads can be compared with the background tectonic loading rates from physical models as well as from earthquake stress drops and recurrence intervals. The tectonic loading rate of the WFZ was estimated at a few to a dozen of kilopascal per year. Bagge et al. (2019) relied on a 3D finite-element model to resolve the interseismic stressing rate at ~19 kPa/yr on the central WFZ, ~12–14 kPa/yr on the WVFZ, and ~13–17 kPa/yr on the East Great Salt Lake Fault Zone. Verdecchia et al. (2019) used a dislocation model to estimate a stressing rate of ~3.6 kPa/yr at 13-km and ~2.3 kPa/yr at 12-km depth. Such loading rates are comparable to those estimated for the San Andreas fault system in California (e.g., Loveless & Meade, 2011; Parsons, 2002), even though the deformation and background seismicity rates in Utah are substantially lower (Chang et al., 2006; Wong et al., 1995). The model-derived tectonic stressing rate strongly depends on the model configurations, including assumptions about past rupture segment boundaries, floating earthquakes, and multisegment ruptures (DuRoss et al., 2016), which will inevitably result in uncertainties. The above-mentioned differences in existing interpretation and uncertainties led us to apply a simple back-of-the-envelope estimate. We consider a typical stress drop of 1–30 MPa in the central United States (Huang et al., 2017) and the recurrence interval on the SLC segment of the WFZ of ~1,300 years (DuRoss & Hylland, 2015; DuRoss et al., 2016), suggesting a tectonic stressing rate of 0.77–23.08 kPa/year.

The tailings-induced $\Delta\sigma_c$ rate has been maintained at about −0.8 kPa/yr (west dip) or 0.8 kPa/yr (east dip) at the hypocentral zone of M5.7 event for about the last three decades. Overall, the tailings load can generate stressing rates that are a factor of 0.03–1.04 of those from tectonic loading. Thus, the anthropogenic load could potentially delay or accelerate event occurrences in the Wasatch fault system by several hundred years, depending on the fault geometry, the frictional coefficient, and the exact receiver location.

4.3. Linking Loads to Seismicity

Although the spatial correlation between the tailings pond and the M5.7 earthquake sequence (Figure 3) and the long existing local seismicity at cluster *W* (Figure 4b) is compelling, the stress distribution due to the ore deposition is indefinite depending on various factors including the receiver fault geometry and the effective coefficient of friction. High-angle normal faults at the Wasatch front appear to shallow into a listric geometry at a depth of 8–12 km as revealed by seismic reflection profiling (e.g., Velasco et al., 2010). The M5.7 earthquake is considered to have ruptured a patch on the deep listric portion of the WFZ dipping to the west (e.g., Pang et al., 2020). However, we cannot rule out the possibility of other seismogenic structures with distinct orientations in the hanging wall of the M5.7 event hosting some of the long-standing small earthquakes and aftershocks. The Saltair structure was originally inferred to be east-dipping from the distribution of aftershocks of the 1962 event and a gravity low around cluster *W* (Wong et al., 1995). In the reanalysis of the legacy gravity data, together with surficial geologic mapping, structural cross sections, deep borehole data, and seismic data, Kleber et al. (2020) reaffirmed this interpretation of the Saltair graben. They proposed a connection between the east-dipping western bounding fault of the Saltair graben and the SE-dipping Harkers fault to the south. Nonetheless, the detailed fault geometries of the Saltair structure and their current activity remain unknown.

It is possible that the triggered slips on the conjugate faults hosting those events can, in turn, add more local loads to the west-dipping Wasatch fault. Similar fault complexity has been observed at the Alto Tiberina fault in Italy, where shallow high-angle structures have been invoked to accommodate deformation around a low-angle normal fault that acts as a basal detachment (Chiaraluce et al., 2007; Vuan et al., 2020). For either nodal planes observed in the M5.7 and its larger aftershocks, the principal earthquake cluster *W* falls in the marginal zone of the $\Delta\sigma_c$ decrease (west-dipping scenario) or increase (east-dipping scenario) by tens of kPa, and the $\Delta\sigma_c$ rate amounts to ∼0.8 kPa/yr at the 9-km seismogenic depth. Where the tailings-induced stress changes are aligned with the background tectonic loading and slip on the WFZ, the tailings load would have been able to alter the time of eventual ruptures. However, a case for delay or hastening of individual events cannot be made in the complicated and unconfirmed shallow and deep fault strands with diverse geometries.

Although WVFZ earthquakes are likely synchronous with or triggered shortly after WFZ earthquakes (DuRoss & Hylland, 2015), their interconnection remains puzzling. Two independent clusters, the eastern, shallower one around the WVFZ and the western, deeper one around the listric WFZ (e.g., Figures 3 and 4). The M5.7 event and its aftershocks suggest these two clusters are connected, possibly through slow slip (e.g., Pollitz et al., 2021; Xue et al., 2018), conservation effect of the antithetic WVFZ (DuRoss & Hylland, 2015; Velasco et al., 2010), and/or pore pressure diffusion along the faults (e.g., Freed, 2005; Goebel & Brodsky, 2018). The aftershock cluster *E* at a shallower depth east of the hypocenter may have been activated by the static stress change (Pang et al., 2020) or afterslip (Pollitz et al., 2021) of the mainshock. Additionally, a delayed activation of aftershocks in cluster *E* by about one week might relate to a permeable fault system allowing for pore pressure diffusion along the fault zone and associated effective normal-stress reduction. The overlying tailings pond, the aquifer system, and/or the nearby lake and river may serve as a source of fluids at greater depths (Hu & Bürgmann, 2020). Clusters *E* & *W* occurred in the proximity of the WFZ and WVFZ, where multiple fault splays may intersect, making it challenging to explicitly address the interplay of the potential hydromechanical coupling.

In the well-instrumented SLC region, none of the basin-wide clusters (Figure 9c) or the state-wide seismicity (Figures S2–S5 in Supporting Information S1) represent clear annual periodicity as observed in other hydrologically driven seismotectonic settings such as the Himalayas (Bettinelli et al., 2008) and California (Amos et al., 2014; Johnson et al., 2017). While Utah contains the largest inland body of saltwater in the Western Hemisphere, the Great Salt Lake and its tributary the Utah Lake, together with seasonally varying hydrological forcing from soil moisture and snow, we do not find statistically significant seasonal seismic activity. This may be due to the spatio-temporally complex loads and the associated diffusion processes producing both failure-encouraging and discouraging stress changes on the Wasatch fault system, throughout the year. Improved seismicity catalogs,

more accurate observations/models of hydrological components including snow and soil moisture, and knowledge of fault geometries in the region are required to better understand such modulation.

Utah earthquake catalogs and Great Salt Lake level observations allow us to make some qualitative comparisons of surface loads and declustered seismicity on a regional scale (Figure 2). Historical large events ($M > \sim 6$) in Utah occurred in the early 1990s and middle 1930s when the lake level reached lows. Modern-day seismographic networks started in 1974 for this region (Wong et al., 1995). Intriguingly, an evident seismic quiescence in the middle 1980s and the following increasing number of earthquakes from the late 1980s to early 1990s coincide with peak water levels and rapidly declining levels, respectively (Figure S6 in Supporting Information S1). However, in the last two decades we see little correlation between multi-annual variations in lake levels and seismicity rates (e.g., lake level declined by 3 m between 2000 and 2005 with no apparent anomalies in seismicity). We note that the increase-peak-decrease trend of the Great Salt Lake levels inversely correlates with the decrease-trough-increase trend of the ore mass during 1981–1995. We believe that the mine production was reduced due to inclement weather during wet years.

Challenges to consistent earthquake detection and characterization may stem from repeated seismic network updates with newly deployed and retired stations through the years and occasional mining-induced events. In addition, the triggering relationship between external loads and seismicity may involve time-dependent processes such as pore-pressure diffusion and slow fault slip. Heterogeneity in porosity and permeability of rocks and fault zones may establish multiple flow paths and thus multiple phases of pore pressure arrivals, which may further regulate the temporal behavior of this critical fault zone. Given these challenges, it is difficult to establish a clear role of external driving forces in seismicity rate changes.

5. Concluding Remarks

The March 18, 2020 Magna earthquake and its aftershocks, as well as clusters of microseismicity during the past four decades, occurred just east of a mine tailings impoundment, where a total of 2.94 billion tons of ore waste were deposited since the early twentieth century. The mine tailings load produced stress changes in the surficial crust exceeding one hundred kPa. We model the cumulative Coulomb stress changes due to aggregate ore deposition since the 1900s near the seismic clusters. The tailings-induced Coulomb stressing rates at seismogenic depths can reach values comparable to those from the background tectonic loading in the SLC region. Nonetheless, the sign and magnitude of the stress changes strongly vary over short distances with the considered fault geometry and friction coefficient. Given the complicated and undetermined fault architecture, no definite conclusion can be reached on the role of elastic tailings loads on the local seismicity. Hydrological loads from the Great Salt Lake, Utah Lake, local aquifer, regional soil moisture and snow generate largely seasonal and low-amplitude stress changes that produce no evident seasonal signature in local and regional seismicity. To improve our understanding of the connection between the anthropogenic and natural surface loads and seismicity, we require better knowledge of the geometries of small and large faults, the magnitude and rate of tectonic stress, and the 3D elastic and poroelastic structure of the lithosphere. Interdisciplinary efforts exploring geotechnical, geophysical, geodetic, and seismic data and models are warranted for a better understanding of such mechanical interactions and for appropriate mitigation measures.

Data Availability Statement

The Pylith code (Aagaard et al., 2013) is available at the Computational Infrastructure for Geodynamics (http://geodynamics.org/cig/software/pylith/).

Acknowledgments
The authors thank University of Utah Seismograph Stations (UUSS) for providing earthquake catalogs (https://quake.utah.edu/earthquake-information-products/earthquake-catalogs); Utah Automated Geographic Reference Center (AGRC) for providing the location of Quaternary faults (https://gis.utah.gov/data/geoscience/quaternary-faults/); U.S. Geological Survey (USGS) for providing the Great Salt Lake levels (https://waterdata.usgs.gov/ut/nwis/uv/?site_no=10010000); Bureau of Reclamation for providing the Utah Lake levels (https://www.usbr.gov/rsvrWater/HistoricalApp.html); NOAA National Weather Service's National Operational Hydrologic Remote Sensing Center (NOHRSC; NOHRSC, 2004) for providing the snow water equivalent estimates in the SNOw Data Assimilation System (SNODAS) (https://www.nohrsc.noaa.gov/archived_data/); NASA Goddard Earth Sciences Data and Information Services Center (GES DISC) for providing the soil moisture and snow water equivalent estimates for validation in North American Land Data Assimilation System (NLDAS) (https://disc.gsfc.nasa.gov/datasets/NLDAS_NOAH0125_M_002/summary?keywords=NLDAS); UVAVCO for providing GPS velocities for the eastern Basin-Range province (https://www.unavco.org/data/gps-gnss/gps-gnss.html); National Agriculture Imagery Program (NAIP) for providing the aerial imagery (https://datagateway.nrcs.usda.gov/GDGHome_DirectDownLoad.aspx).

References

Aagaard, B., Kientz, S., Knepley, M., Strand, L., & Williams, C. (2013). *Pylith user manual: Version 2.1. 0*. Computational Infrastructure of Geodynamics.

Amos, C. B., Audet, P., Hammond, W. C., Bürgmann, R., Johanson, I. A., & Blewitt, G. (2014). Uplift and seismicity driven by groundwater depletion in central California. *Nature*, *509*, 483–486. https://doi.org/10.1038/nature13275

Ampuero, J.-P., Billant, J., Brenguier, F., Cavalié, O., Courboulex, F., Deschamps, A., et al. (2020). The November 11 2019 Le Teil, France M5 earthquake: A triggered event in nuclear country. *EGU General Assembly 2020*. Online, 4–8 May 2020. https://doi.org/10.5194/egusphere-egu2020-18295

Arabasz, W. J., Pechmann, J. C., & Brown, E. D. (1992). Observational seismology and the evaluation of earthquake hazards and risk in the Wasatch Front area, Utah. In W. W. Hays, & P. L. Gori (Eds.), *Assessment of regional earthquake hazards and Risk along the Wasatch front* (pp. D1–D36). U.S. Geological Survey Professional Paper.

Argus, D. F., Fu, Y., & Landerer, F. W. (2014). Seasonal variation in total water storage in California inferred from GPS observations of vertical land motion. *Geophysical Research Letters*, *41*, 1971–1980. https://doi.org/10.1002/2014gl059570

Bagge, M., Hampel, A., & Gold, R. D. (2019). Modeling the Holocene slip history of the Wasatch fault (Utah): Coseismic and postseismic Coulomb stress changes and implications for paleoseismicity and seismic hazard. *GSA Bulletin*, *131*(1–2), 43–57. https://doi.org/10.1130/b31906.1

Baker, B., Holt, M. M., Pankow, K. L., Koper, K. D., & Farrell, J. (2021). Monitoring the 2020 Magna, Utah, Earthquake Sequence with Nodal Seismometers and Machine Learning. *Seismological Research Letters*, *92*(2A), 787–801. https://doi.org/10.1785/0220200316

Bettinelli, P., Avouac, J.-P., Flouzat, M., Bollinger, L., Ramillien, G., Rajaure, S., & Sapkota, S. (2008). Seasonal variations of seismicity and geodetic strain in the Himalaya induced by surface hydrology. *Earth and Planetary Science Letters*, *266*, 332–344. https://doi.org/10.1016/j.epsl.2007.11.021

Bills, B. G., Currey, D. R., & Marshall, G. A. (1994). Viscosity estimates for the crust and upper mantle from patterns of lacustrine shoreline deformation in the Eastern Great Basin. *Journal of Geophysical Research*, *99*, 22059–22086. https://doi.org/10.1029/94jb01192

Bowman, S. D., & Arabasz, W. J. (2017). *Utah earthquakes (1850–2016) and Quaternary faults*. Utah Geological Survey Map 277. Retrieved from https://ugspub.nr.utah.gov/publications/maps/m-277.pdf

Chang, W.-L., Smith, R. B., Meertens, C. M., & Harris, R. A. (2006). Contemporary deformation of the Wasatch Fault, Utah, from GPS measurements with implications for interseismic fault behavior and earthquake hazard: Observations and kinematic analysis. *Journal of Geophysical Research*, *111*. https://doi.org/10.1029/2006jb004326

Chiaraluce, L., Chiarabba, C., Collettini, C., Piccinini, D., & Cocco, M. (2007). Architecture and mechanics of an active low-angle normal fault: Alto Tiberina Fault, northern Apennines, Italy. *Journal of Geophysical Research*, *112*, B10310. https://doi.org/10.1029/2007jb005015

Costain, J. K., & Bollinger, G. A. (2010). Review: Research Results in Hydroseismicity from 1987 to 2009. *Bulletin of the Seismological Society of America*, *100*(5A), 1841–1858. https://doi.org/10.1785/0120090288

Craig, T. J., Chanard, K., & Calais, E. (2017). Hydrologically-driven crustal stresses and seismicity in the New Madrid Seismic Zone. *Nature Communications*, *8*, 2143. https://doi.org/10.1038/s41467-017-01696-w

DuRoss, C. B., & Hylland, M. D. (2015). Synchronous ruptures along a major graben-forming fault system—Wasatch and West Valley fault zones, Utah, USA. *Bulletin of the Seismological Society of America*, *105*, 14–37. https://doi.org/10.1785/0120140064

DuRoss, C. B., & Lund, W. R. (2013). *Sleeping giant—The earthquake threat facing Utah's Wasatch Front* (p. 20). Seismological Society of America 2013 Annual Meeting, Field Trip Guide.

DuRoss, C. B., Personius, S. F., Crone, A. J., Olig, S. S., Hylland, M. D., Lund, W. R., & Schwartz, D. P. (2016). Fault segmentation: New concepts from the Wasatch Fault Zone, Utah, USA. *Journal of Geophysical Research: Solid Earth*, *121*, 1131–1157. https://doi.org/10.1002/2015jb012519

Dziewonski, A. M., & Anderson, D. L. (1981). Preliminary reference Earth model. *Physics of the Earth and Planetary Interiors*, *25*(4), 297–356. https://doi.org/10.1016/0031-9201(81)90046-7

Ellsworth, W. (2013). Injection-Induced Earthquakes. *Science*, *341*. https://doi.org/10.1126/science.1225942

Freed, A. M. (2005). Earthquake triggering by static, dynamic, and postseismic stress transfer. *Annual Review of Earth and Planetary Sciences*, *33*, 335–367. https://doi.org/10.1146/annurev.earth.33.092203.122505

Ge, S., Liu, M., Lu, N., Godt, J. W., & Luo, G. (2009). Did the Zipingpu reservoir trigger the 2008 Wenchuan earthquake? *Geophysical Research Letters*, *36*, L20315. https://doi.org/10.1029/2009gl040349

Gilbert, G. K. (1890). Lake Bonneville. *United States Geological Survey Monographs*, *1*, 438.

Goebel, T. H. W., & Brodsky, E. E. (2018). The spatial footprint of injection wells in a global compilation of induced earthquake sequences. *Science*, *361*(6405), 899–904. https://doi.org/10.1126/science.aat5449

González, P., Tiampo, K., Palano, M., Cannavó, F., & Fernández, J. (2012). The 2011 Lorca earthquake slip distribution controlled by groundwater crustal unloading. *Nature Geoscience*, *5*, 821–825.

Gupta, H. K. (2002). A review of recent studies of triggered earthquakes by artificial water reservoirs with special emphasis on earthquakes in Koyna, India. *Earth-Science Reviews*, *58*(3–4), 279–310. https://doi.org/10.1016/s0012-8252(02)00063-6

Gwynn, J. W. (1996). Commonly asked questions about Utah's Great Salt Lake and ancient Lake Bonneville. *Utah Geological Survey, Public Information Series*, *39*, 22.

Hardebeck, J. L., Nazareth, J. J., & Hauksson, E. (1998). The static stress change triggering model: Constraints from two southern California earthquake sequences. *Journal of Geophysical Research*, *103*, 24427–24437. https://doi.org/10.1029/98jb00573

Harris, R. A., & Simpson, R. W. (1992). Changes in static stress on southern California faults after the 1992 Landers earthquake. *Nature*, *360*, 251–254. https://doi.org/10.1038/360251a0

Herring, T. A., Melbourne, T. I., Murray, M. H., Floyd, M. A., Szeliga, W. M., King, R. W., et al. (2016). Plate Boundary Observatory and related networks: GPS data analysis methods and geodetic products. *Reviews of Geophysics*, *54*. https://doi.org/10.1002/2016rg000529

Herrmann, R. B., Benz, H., & Ammon, C. J. (2011). Monitoring the earthquake source process in North America. *Bulletin of the Seismological Society of America*, *101*, 2609–2625. https://doi.org/10.1785/0120110095

Hetzel, R., & Hampel, A. (2005). Slip rate variations on normal faults during glacial–interglacial changes in surface loads. *Nature*, *435*, 81–84. https://doi.org/10.1038/nature03562

Hu, X., & Bürgmann, R. (2020). Aquifer deformation and active faulting in Salt Lake Valley, Utah, USA. *Earth and Planetary Science Letters*, *547*. https://doi.org/10.1016/j.epsl.2020.116471

Hu, X., Lu, Z., & Wang, T. (2018). Characterization of hydrogeological properties in Salt Lake Valley, Utah using InSAR. *Journal of Geophysical Research: Earth Surface*, *123*. https://doi.org/10.1029/2017jf004497

Hu, X., Oommen, T., Lu, Z., Wang, T., & Kim, J. W. (2017). Consolidation settlement of Salt Lake County tailings impoundment revealed by time-series InSAR observations from multiple radar satellites. *Remote Sensing of Environment*, *202*, 199–209. https://doi.org/10.1016/j.rse.2017.05.023

Huang, Y., Ellsworth, W. L., & Beroza, G. C. (2017). Stress drops of induced and tectonic earthquakes in the central United States are indistinguishable. *Science Advances*, *3*(8), e1700772. https://doi.org/10.1126/sciadv.1700772

Johanson, I. A., & Bürgmann, R. (2010). Coseismic and postseismic slip from the 2003 San Simeon earthquake and their effects on backthrust slip and the 2004 Parkfield earthquake. *Journal of Geophysical Research*, *115*, B07411. https://doi.org/10.1029/2009jb006599

Johnson, C. W., Fu, Y., & Bürgmann, R. (2017). Seasonal water storage, stress modulation, and California seismicity. *Science*, *356*(6343), 1161–1164. https://doi.org/10.1126/science.aak9547

Johnson, C. W., Fu, Y., & Bürgmann, R. (2020). Hydrospheric modulation of stress and seismicity on shallow faults in southern Alaska. *Earth and Planetary Science Letters*, *530*, 115904. https://doi.org/10.1016/j.epsl.2019.115904

Kleber, E. J., McKean, A. P., Hiscock, A. I., Hylland, M. D., Hardwick, C. L., McDonald, G. N., et al. (2020). Geologic setting, ground effects, and proposed structural model for the 18 March 2020 Mw 5.7 Magna, Utah, Earthquake. *Seismological Research Letters*, *92*(2A), 710–724. https://doi.org/10.1785/0220200331

Krahulec, K. (2018). Production history of the Bingham mining district, Salt Lake County, Utah - an update. Preprint. https://doi.org/10.13140/RG.2.2.28618.00966

Lay, T., & Wallace, T. C. (1995). *Modern global Seismology*. Academic Press (ISBN: #0-12-732870-X).

Li, T., Cai, M. F., & Cai, M. (2007). A review of mining-induced seismicity in China. *International Journal of Rock Mechanics and Mining Sciences*, *44*(8), 1149–1171. https://doi.org/10.1016/j.ijrmms.2007.06.002

Loveless, J., & Meade, B. (2011). Partitioning of localized and diffuse deformation in the Tibetan Plateau from joint inversions of geologic and geodetic observations. *Earth and Planetary Science Letters*, *303*(1–2), 11–24. https://doi.org/10.1016/j.epsl.2010.12.014

Mitchell, K. E., Lohmann, D., Houser, P. R., Wood, E. F., Schaake, J. C., Robock, A. et al. (2004). The multi-institution North American Land Data Assimilation System (NLDAS): Utilizing multiple GCIP products and partners in a continental distributed hydrological modeling system. *Journal of Geophysical Research*, *109*, D07S90. https://doi.org/10.1029/2003jd003823

National Operational Hydrologic Remote Sensing Center (NOHRSC). (2004). *Snow data Assimilation system (SNODAS) data products at NSIDC*. National Snow and Ice Data Center.

Pang, G., Koper, K. D., Mesimeri, M., Pankow, K. L., Baker, B., Farrell, J., et al. (2020). Seismic Analysis of the 2020 Magna, Utah, Earthquake Sequence: Evidence for a Listric Wasatch Fault. *Geophysical Research Letters*, *47*, e2020GL089798. https://doi.org/10.1029/2020gl089798

Pankow, K. L., Moore, J. R., Hale, J. M., Koper, K. D., Kubacki, T., Whidden, K. M., & McCarter, M. K. (2014). Massive landslide at Utah copper mine generates wealth of geophysical data. *Geological Society of America Today*, *24*(1). https://doi.org/10.1130/gsatg191a.1

Parsons, T. (2002). Post-1906 stress recovery of the San Andreas fault system calculated from three-dimensional finite element analysis. *Journal of Geophysical Research*, *107*(B8), 2162. https://doi.org/10.1029/2001jb001051

Pollitz, F. F., Wicks, C. W., & Svarc, J. L. (2021). Coseismic fault slip and afterslip associated with the 18 March 2020 M 5.7 Magna, Utah, Earthquake. *Seismological Research Letters*, *92*, 741–754. https://doi.org/10.1785/0220200312

Qian, Y., Chen, X., Luo, H., Wei, S., Wang, T., Zhang, Z., & Luo, X. (2019). An extremely shallow Mw4.1 thrust earthquake in the eastern Sichuan Basin (China) likely triggered by unloading during infrastructure construction. *Geophysical Research Letters*, *46*, 775. https://doi.org/10.1029/2019gl085199

Rubinstein, J. L., & Mahani, A. B. (2015). Myths and facts on wastewater injection, hydraulic fracturing, enhanced oil recovery, and induced seismicity. *Seismological Research Letters*, *86*(4), 1060–1067. https://doi.org/10.1785/0220150067

Talwani, P. (1997). On the nature of reservoir-induced seismicity. *Pure and Applied Geophysics*, *150*, 473–492. https://doi.org/10.1007/s000240050089

Tinto, R. (2019). Tailings Impoundment. Retrieved from https://riotintokennecott.com/wp-content/uploads/2019/05/Tailings.pdf accessed May 2020.

UUSS [@UUSSquake]. (2020a). *This conceptual model illustrates one possible scenario for the location of the M5.7 Magna earthquake and its aftershocks relative to the Wasatch fault and associated faults*. [Tweet]. Retrieved from https://twitter.com/UUSSquake/status/1243552563762360320

UUSS [@UUSSquake]. (2020b). *To the Science Community: Relocations of the aftershocks from March 18 through March 24 indicate that the Magna earthquake ruptured a west dipping fault, which is part of the Wasatch Fault system. The cross-section shows the location of the mainshock and aftershocks*. [Tweet]. Retrieved from https://twitter.com/UUSSquake/status/1243257902170685440

Velasco, M. S., Bennett, R. A., Johnson, R. A., & Hreinsdottir, S. (2010). Subsurface fault geometries and crustal extension in the eastern Basin and Range province, western U.S. *Tectonophysics*, *488*, 131–142. https://doi.org/10.1016/j.tecto.2009.05.010

Verdecchia, A., Carena, S., Pace, B., & DuRoss, C. B. (2019). The effect of stress changes on time-dependent earthquake probabilities for the central Wasatch fault zone, Utah, USA. *Geophysical Journal International*, *219*(2), 1065–1081. https://doi.org/10.1093/gji/ggz336

Vuan, A., Brondi, P., Sugan, M., Chiaraluce, L., Di Stefano, R., & Michele, M. (2020). Intermittent slip along the Alto Tiberina low-angle normal fault in central Italy. *Geophysical Research Letters*, *47*, e2020GL089039. https://doi.org/10.1029/2020gl089039

Wetzler, N., Shalev, E., Göbel, T., Amelung, F., Kurzon, I., Lyakhovsky, V., & Brodsky, E. E. (2019). Earthquake swarms triggered by groundwater extraction near the Dead Sea Fault. *Geophysical Research Letters*, *46*, 8056–8063. https://doi.org/10.1029/2019gl083491

Whidden, K. M., & Pankow, K. L. (2012). A Catalog of Regional Moment Tensors in Utah from 1998 to 2011. *Seismological Research Letters*, *83*(5). https://doi.org/10.1785/0220120046

Wiemer, S. (2001). A software package to analyze seismicity: ZMAP. *Seismological Research Letters*, *72*(3), 373–382. https://doi.org/10.1785/gssrl.72.3.373

Wong, I., Olig, S., Green, R., Moriwaki, Y., Abrahamson, N., Baures, D., et al. (1995). *Seismic Hazard Evaluation of the Magna Tailings Impoundment. Environmental and Engineering Geology of the Wasatch Front Region* (Vol. 24, pp. 95–110). Utah Geological Association Publication.

Xue, L., Bürgmann, R., Shelly, D. R., Johnson, C. W., & Taira, T. (2018). Kinematics of the 2015 San Ramon, California earthquake swarm: Implications for fault zone structure and driving mechanisms. *Earth and Planetary Science Letters*, *489*, 135–144. https://doi.org/10.1016/j.epsl.2018.02.018

Xue, L., Johnson, C. W., Fu, Y., & Bürgmann, R. (2020). Seasonal seismicity in the western branch of the East African Rift System. *Geophysical Research Letters*, *47*, e2019GL085882. https://doi.org/10.1029/2019gl085882